Low Temperature p-type Microcrystalline Silicon as Carrier Selective Contact for Silicon Heterojunction Solar Cells

Angela N. Fioretti, *Member, IEEE,* Mathieu Boccard, *Member, IEEE,* Raphaël Monnard, and Christophe Ballif, *Member, IEEE*

***Abstract*—Silicon heterojunction (SHJ) solar cells have reached record efficiency, particularly in all-back-contacted architectures. Despite this, two-side contacted SHJ cells still suffer from parasitic absorption and series resistance losses in the amorphous silicon contacts. An alternative to the doped amorphous silicon layer is microcrystalline silicon, which exhibits improved transparency and charge transport while maintaining the superior passivation quality of all-silicon contact stacks. However, depositing thin, highly crystalline films has remained a challenge until recently. In this work, we use deposition temperatures <200 °C to improve the performance of p-type μc-Si:H contact layers. With these layers, we demonstrate J_{sc} gains of 1 mA/cm^2, while reducing series resistance below 1 Ωcm^2, leading to screen-printed 4 cm^2 cells with certified $\eta = 23.45\%$. Using a suite of device and material characterization techniques, we show that reduced deposition temperature leads to an increase in crystalline volume fraction from 35% to 55% for p-type films, which mitigates parasitic absorption in the front contact and facilitates hole extraction. These improvements are explained as resulting from higher transparency in the p-type layer accompanied by higher band bending in the c-Si wafer. These findings provide a method to improve SHJ solar cells performance, while offering insight into the importance of band bending considerations when optimizing heterojunction designs.**

***Index Terms*—silicon heterojunction solar cells, microcrystalline, carrier selective contacts, parasitic absorption, series resistance.**

I. Introduction

HETEROJUNCTION-based silicon solar cells hold the world record in efficiency for silicon photovoltaics. Full-area surface passivation allows cells of this type to reach high open-circuit voltages (Voc) upwards of 730 mV [1], leading to efficiencies >26% when using all-back-contacted designs [2]. However, classical silicon heterojunction (SHJ) cell efficiency has been limited to 25.1% due to losses from both parasitic absorption in the hydrogenated amorphous silicon (a-Si:H) contact layers and increased series resistance (R_s) [3]. To benefit from the reduced process complexity of two-side contacted SHJ architectures, recent research efforts have focused on developing contact materials that could be both more transparent than a-Si:H and/or improve doped layer conductivity [4]–[10]

The authors are with the Photovoltaics and Thin Film Electronics Laboratory, Institute of Microengineering, École Polytechnique Fédérale de Lausanne (EPFL), Rue de la Maladière 71b, CH-2000 Neuchâtel, Switzerland e-mail: mathieu.boccard@epfl.ch

Manuscript received Month XX, 2019; revised Month XX, 2019.

Contacts utilizing microcrystalline silicon (μc-Si:H) doped layers represent an excellent compromise between the passivation quality of all-Si contact stacks and the reduced parasitic absorption of more transparent materials. By leveraging the indirect nature of the crystalline silicon bandgap, μc-Si:H contact layers exhibit improved transparency compared to their amorphous counterparts. Indeed, this strategy has received attention in the literature [5], [11]–[13], but difficulties in depositing highly crystalline layers thin enough to realize a reduction in parasitic absorption have persisted. Publication of an effective pretreatment method for seeding microcrystalline growth on amorphous passivation layers has been a key development in the deposition of thin, p-type μc-Si:H films [14], [15].

Here, we demonstrate that by combining the pretreatment method of previous work with growth temperatures below 200°C, further crystallinity gains in p-type μc-Si contact layers can be achieved. By applying these layers to SHJ solar cells, we demonstrate gains on all aspects of solar cell performance (J_{sc}, V_{oc}, FF, and η), and achieve an optimized SHJ solar cell with certified $\eta = 23.45\%$. Using Raman spectroscopy and external quantum efficiency measurements, we show that short wavelength efficiency gains are directly related to increased crystallinity in the p-type contact. Based on electrical and optical characterization of p-type μc-Si:H, coupled with temperature- and illumination-dependent current-voltage measurements, we attribute this R_s reduction to higher band bending in the c-Si wafer resulting from a higher workfunction in the p-type microcrystalline layer. Overall, these results offer insight into band bending considerations for heterojunction designs, and provide a widely applicable method by which to improve the performance of SHJ solar cells.

II. Methods

A. Solar Cell Fabrication and Characterization

Solar cells were prepared on textured, 4", n-type float-zone wafers with resistivity of 2–3 Ωcm, and thickness of 180–220 μm. Plasma-enhanced chemical vapor deposition (PECVD) was used to deposit all thin film silicon layers. Doped p- or n-type μc-Si:H contact layers were deposited in the same chamber at a frequency of 40.68 MHz at each of the following temperatures: 200°C, 175°C, 150°C, or 125°C. Intrinsic a-Si:H for surface passivation was deposited in a

separate chamber at a fixed temperature of 200°C for all cells. Dopant gases used for the silicon contact layers were tri-methyl boron (TMB) for p-type and PH_3 for n-type. The thickness of the doped μc-Si:H layers was 40 nm on glass, which is known from previous calibration measurements to yield ∼27 nm on the textured wafer. A plasma pre-treatment to oxidize the surface of the intrinsic a-Si:H was applied prior to the p-type μc-Si:H layer deposition in all cells, as described in more detail elsewhere [15]. Tin-doped indium oxide (ITO) was deposited by sputtering (through a shadow mask on the front and full-area on the back) and silver was sputtered (full area) on the back. A silver grid was then screen-printed on the front to complete five, 4 cm^2 solar cells. Wafers were then annealed at 210°C for 20 minutes in air.

Current-voltage characteristics (JV) were collected on finished devices using a Wacom Electric Co. Super solar simulator with AM 1.5G illumination and Keithley sourcemeters. For series resistance extraction, JV characteristics for each cell were collected at 5% illumination to obtain a curve in which V_{oc} approached V_{mpp} for the 1 sun illumination curve. By linear translation of the 5% illumination curve downward to coincide with the curve collected at 1 sun, the difference between $V_{oc}^{5\%}$ and the corresponding voltage (V_A) at the same current value on the 1 sun JV curve could be determined, and used to calculate R_s in Equation 1.

External quantum efficiency (EQE) was collected using a home-built spectral response measurement system, equipped with xenon arc lamp. Temperature- and illumination-dependent JV measurements used for extracting fill factor in Figure 4a were performed on a custom-built solar simulator equipped with combined halogen/LED arrays, PID temperature controller, and Peltier heating/cooling elements. Temperature was measured by a PT-100 temperature probe positioned directly beneath the cells inside the vacuum chuck during measurement. Simulated FF and activation energy values in Fig. 5 and band diagrams in Figure 6 were constructed using the PC1D software package [16]. Finally, after optimization, one champion cell was submitted to the Institute for Solar Energy Research GmbH (ISFH) in Emmerthal, Germany for certification.

B. Material Characterization

Crystalline volume fraction of doped μc-Si:H layers was measured directly on each cell by Raman spectroscopy using 325 nm light to avoid contributions from the wafer. Resulting spectra were fit with three Gaussian curves centered at 480 cm^{-1}, 510 cm^{-1} and 520 cm^{-1} [17]. Dark conductivity measurements of ∼40 nm thick p-type μc-Si:H layers on intrinsic a-Si:H-coated glass were carried out in a nitrogen atmosphere at an approximate pressure of 1 mbar. Temperature was ramped from 25 °C to 180 °C over 15 minutes, held for 90 minutes, and then ramped down to 25 °C over 150 minutes, with resistance measurements taken during both heating and cooling. Activation energy was determined from the slope of the linear portion of the cooling curve using an Arrhenius relationship, and conductivity at 25°C was determined using the thickness values mentioned above, which were obtained from ellipsometry.

Variable-angle spectroscopic ellipsometry was performed on p-type μc-Si:H on glass deposited at each temperature over the energy range 0.6–6 eV at angles of 50°, 60°, and 70°. Spectra were collected using a Horiba Jobin Yvon ellipsometer, and modeling was performed in the DeltaPsi2 software. More details on ellipsometry fitting are given in Appendix A. Transmission spectra were collected for the same p-type μc-Si:H films on glass as measured by ellipsometry using a Perkin Elmer Lambda 950 UV/VIS/NIR spectrometer over the wavelength range 250–2000 nm. These transmission spectra were used in the bound-multi model ellipsometry fits described in Appendix A.

III. Results and Discussion

We begin by presenting current-voltage (JV) characteristics and associated figures-of-merit (Figure 1) for SHJ solar cells fabricated with doped μc-Si:H contact layers (both n- and p-type) deposited at each of four temperatures: 200 °C, 175 °C, 150 °C, and 125 °C. Figure 1(a) displays representative JV curves from each set of five repeated cells. The largest gain in cell performance was achieved when lowering doped layer deposition temperature from 200 °C to 175 °C, while further temperature decreases produced less significant improvements. It should be noted that changing the deposition temperature of both doped layers simultaneously was done in order to simplify cell processing (since both n- and p-type layers were deposited in the same chamber). It was found in preliminary experiments that the greatest effect on cell performance originated from changing the deposition temperature of the p-layer alone, and that only a small additional increase in performance was observed when changing the deposition temperature of both n-type and p-type layers. Figure 1(b–e) summarizes efficiency (η), fill factor (FF), short-circuit current (J_{sc}), and open-circuit voltage (V_{oc}) for all cells in each set, and shows that although J_{sc} increases approximately linearly with decreasing temperature, the other figures-of-merit increase for 175 °C cells and then level off for lower temperature cells.

Figure 1(f) displays series resistance (R_s) extracted from variable illumination JV measurements using the following formula [18]:

$$R_s = \frac{V_{oc(shaded)} - V_A}{J_{sc(full)} - J_{sc(shaded)}} \tag{1}$$

where $shaded$ refers to JV curves measured at 5% of 1 sun illumination, $full$ refers to JV curves measured at 1 sun, and V_A represents the voltage corresponding to the point on the full illumination JV curve at which current is equal to $J_{sc(full)} - J_{sc(shaded)}$. R_s reaches a minimum average of 0.68 Ωcm^2 for 150 °C cells, which is a reduction of approximately 1 Ωcm^2 from the average R_s for 200 °C cells.

Finally, Figure 1(g) presents the percent change of the median value of V_{mpp}, J_{mpp}, V_{oc}, and J_{sc} (the variables contributing to FF) for each set of cells with respect to the same value for 200 °C cells. The largest percent change is observed in V_{mpp} for each set of low temperature cells, with the most pronounced difference being for cells with doped layers deposited at 175 °C.

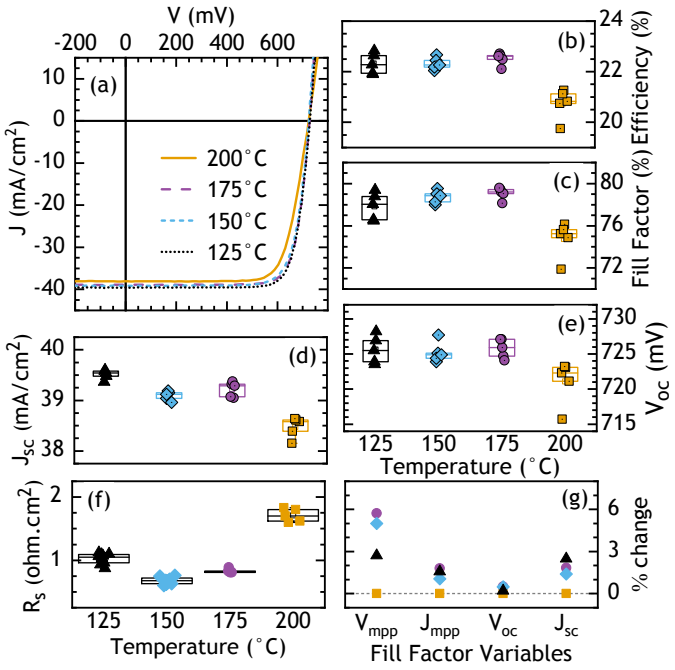

Fig. 1. (a) Representative current-voltage curves for 4 cm^2 SHJ cells with doped μcSi:H layers grown at varying temperature. For each cell, the growth temperature of both the n- and p-type layers was the same. (b)–(e) Efficiency, FF, J_{sc}, and V_{oc} extracted from the JV curves for each of five repeated cells with doped layers deposited at the indicated temperatures. Each figure of merit exhibits an increase for the lower temperature cells compared to the cells prepared at 200°C. (f) Series resistance (R_s) extracted for each set of cells from variable illumination measurements. R_s decreases by up to 1 Ωcm^2 for the lower temperature cells. (g) Percent change of the median value of each component of FF, calculated using the difference of each value from that of 200°C cells. The largest percent change is observed for V_{mpp}, indicating this contributes most to the rise in FF.

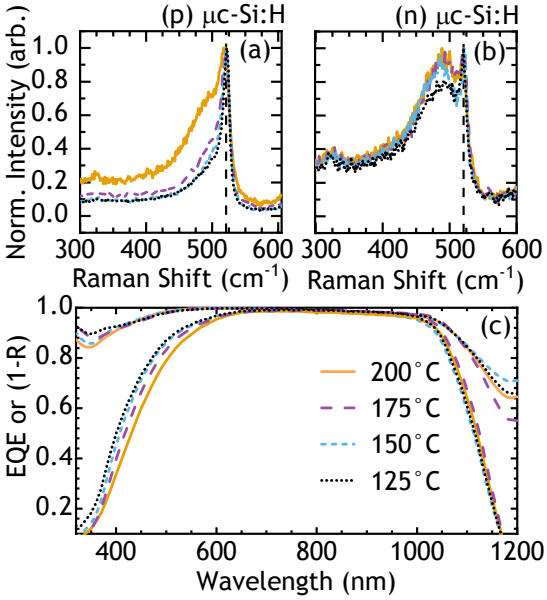

Fig. 2. Normalized Raman spectra for (a) p-type and (b) n-type μc-Si:H layers. Crystalline volume fraction of p-type layers increased from 35% to 55% when deposition temperature was lowered from 200 °C to 175 °C, but remained mostly unchanged for n-type films. (c) EQE and absorptance (1-R) curves for the cells in Figure 1a. Gains in EQE are observed with decreasing deposition temperature over the 320–600 nm wavelength range, despite total absorptance among the four cells being nearly identical, indicative of improved light in-coupling in the lower temperature cells.

Overall, the results shown in Figure 1 highlight two key factors likely contributing to improved cell performance in lower temperature cells. First, the increase in J_{sc} when the doped μc-Si:H contact layers are deposited at <200 °C is indicative of more light in-coupling to the cells, which is consistent with lower parasitic absorption. Second, the reduction in R_s, with associated increase in V_{mpp} and FF, points to improved charge extraction for cells fabricated with lower temperature doped layers. Additionally, the increase in V_{oc} observed for lower temperature cells suggests an increase in field-effect passivation, since chemical passivation from the intrinsic a-Si:H layer is assumed to be the same for all cells. In the following figures, mechanisms underlying each of these factors will be investigated in more detail.

Turning now to Figure 2, we present Raman spectroscopy of doped μc-Si:H layers deposited on cells corresponding to the JV curves shown in Figure 1a, as well as external quantum efficiency (EQE) and absorptance (1-R) of the same cells. In Figure 2a, Raman intensity associated with amorphous material, seen as a shoulder near 480 cm^{-1}, was found to decrease when deposition temperature was lowered below 200 °C for p-type μc-Si:H. However, for n-type layers (Figure 2b) Raman intensity of the amorphous shoulder remains mostly unchanged with lower deposition temperature. Gaussian fits of the spectra in Figure 2a–b were used to extract crystalline volume fraction of the layers, and it was found that for p-type μc-Si:H this value jumped from 35% at 200 °C to 55% at lower deposition temperatures. By contrast, n-type μc-Si:H layers maintained approximately 25% crystalline volume fraction no matter the deposition temperature.

In Figure 2c, EQE profiles of the associated cells exhibit efficiency gains in the 320–600 nm wavelength range. Over this same spectral range, cell total absorptance (top grouping of curves) is essentially identical among the four cells. From 600–1200 nm, EQE was mostly similar for all deposition temperatures, although the 175 °C cell did yield a higher EQE than the others for wavelengths of 1000–1200 nm. We attribute differences in the EQE response over the range 1000–1200 nm to variation in the sheet resistance of the ITO layers, since the cells were prepared in separate batches and the ITO properties are known to vary slightly from run to run. As can be expected, higher crystallinity p-type μc-Si:H layers are more transparent, leading to higher EQE in the blue wavelength region. These findings indicate improved light in-coupling for lower temperature cells compared to those with doped layers deposited at 200 °C. Thus, the observed crystallinity enhancement in the front-side p-type μc-Si:H contacts leads to reduced parasitic absorption.

Figure 3 shows the results of bound multi-model fitting of ellipsometry and UV-Vis-NIR transmission data collected on p-type μc-Si:H layers co-deposited on glass with the cells in Figure 1a. Spectra were fit using the Kato-Adachi dispersion model [19], with layer thickness and resulting material properties as the "bound" variables required to be the same between the models of the transmission and ellip-

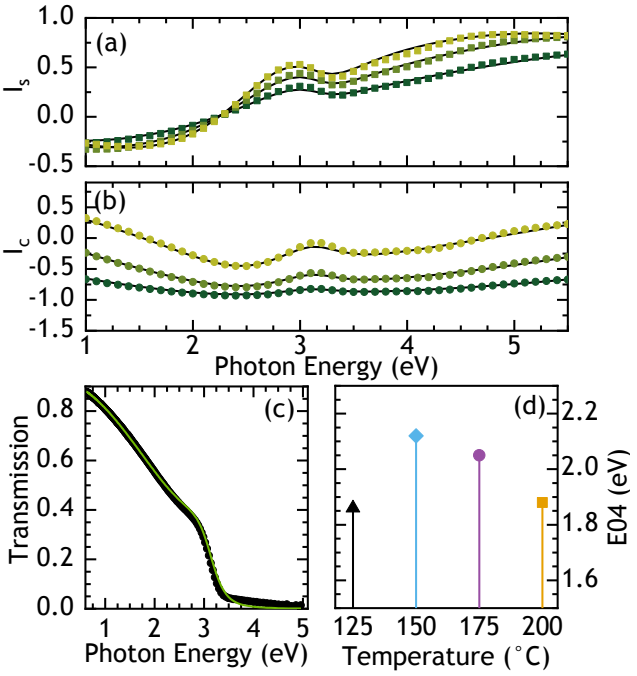

Fig. 3. (a-b) Representative fits of the ellipsometry measurables I_s and I_c (describing the output elliptical polarization state) for a p-type μc-Si:H layer on glass. (c) Representative transmission spectrum with associated fit for the same layer. (d) E_{04} values extracted from the bound multi-models for p-type μc-Si:H. Note the increase in E_{04} for films grown at 175 °C and 150 °C, suggesting a similar shift in absorption onset.

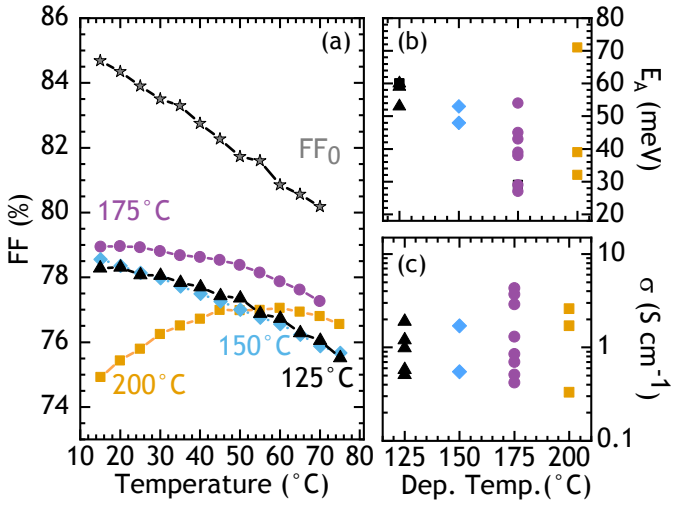

Fig. 4. Fill factor as a function of measurement temperature for representative cells with doped layers deposited at 125 °C–200 °C. Gray stars give the implied fill factor (FF_0) at each measurement temperature for a representative cell with doped layers prepared at 200 °C. For the cells fabricated with low-temperature doped layers, FF does not drop with decreasing temperature, but instead saturates near 79%, consistent with a lower thermal barrier to charge extraction. (b) Activation energy (E_A) and (c) conductivity (σ) from dark conductivity measurements of representative p-type μc-Si:H thin films on glass. E_A and σ do not change significantly with varying growth temperature, despite the increased crystalline fraction for lower temperature films.

sometry spectra. Further details on the dispersion formula, material model, and fit results for each layer are given in Appendix A. Fig. 3a–c display representative fits of the I_s, I_c, and transmission data, respectively. Fig. 3d presents the energy cutoff at which absorption falls below 10^4 cm^{-1} (E_{04}) determined from the fits for each layer. Although E_{04} does not coincide with the absorption onset [20], it provides a reliable way to track the width of the optical bandgap without relying on specific models (such as Tauc's plot) and has been shown previously to be sensitive to changes in the optical bandgap of thin film silicon with varying deposition temperature [21], [22]. For these layers, E_{04} was found to shift to higher energy as deposition temperature decreased to 150 °C, suggesting a similar shift in optical bandgap, which would arise from the more indirect nature of the crystalline silicon bandgap compared to the direct optical transitions in amorphous silicon. This shift in optical bandgap is consistent with both the blue wavelength EQE increase observed in Fig. 2c and the increase in J_{sc} shown in Fig. 1d, and underpins the conclusion that increased crystallinity in the low temperature p-type μc-Si:H layers leads to reduced parasitic absorption.

To investigate the influence of low temperature deposition on improved charge extraction, variable-temperature JV and dark conductivity measurements were performed (Fig. 4). Fig. 4a displays FF as a function of measurement temperature for representative cells corresponding to those presented in Fig. 1. Gray stars give the FF in absence of series resistance (FF_0) at each measurement temperature for a cell prepared at 200 °C, which was calculated using the same method described earlier for determining R_s [18]. Note that FF_0 vs. temperature curves were also collected for lower temperature cells, and it was confirmed that the 200 °C cell is representative of the cells prepared at other temperatures. For the 200 °C cell, FF drops as measurement temperature decreases, with a maximum FF of approximately 77% between 50–60 °C. In the case of lower temperature cells, the same behavior is not observed, instead exhibiting a gain in FF as measurement temperature decreases, up to an apparent saturation near $FF = 79\%$. This finding indicates that the thermal barrier to charge extraction present in cells with μc-Si:H layers deposited at 200 °C is greatly reduced when these layers are deposited at lower temperature. As shown in Fig. 2a-b, lower deposition temperature increased the crystalline volume fraction of the p-μcSi:H layer while the n-type layer remained unchanged, suggesting that the reduced thermal barrier shown in Fig. 4a is largely due to this increased crystallinity and the associated improvement of contact properties in the p-type layer. This conclusion is also consistent with previous work showing the thermal barrier to be suppressed for p-μcSi:H layers compared to p-aSi:H layers in cells of the same architecture [5].

Fig. 4b displays activation energy (E_A) taken from dark conductivity measurements of 3–7 repeated p-type μc-Si:H films deposited on i-aSi:H-coated glass. Films exhibited E_A between 30–60 meV, which is much lower than typical values for p-type a-Si:H (250–400 meV) [23]. Additionally, E_A is similar even when comparing layers of device-relevant thickness (∼40 nm) to very thin layers (∼10 nm), suggesting that all layers are highly crystalline from the beginning of film growth. Conductivity (σ, Fig. 4c) extracted from the same measurements was also similar among the films, in the

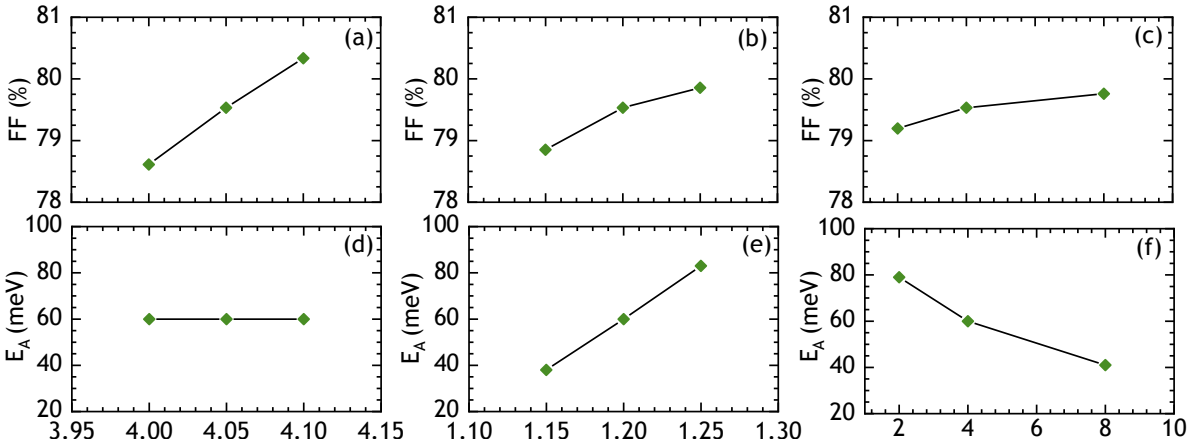

Fig. 5. New figure added. (a)-(c) Variation of FF from PC1D-simulated cells in which the electron affinity, bandgap, or doping concentration in the p-layer was varied, respectively. In all cases, the approximately 2% absolute increase in FF observed in Fig. 1c is well reproduced. (d)-(f) Variation of the activation energy (E_A) of the free-standing p-μcSi:H layer from the same simulations, in which the best representation of the E_A values shown in Fig. 4b is obtained for a widening bandgap.

range 0.5–5 Scm^{-1} no matter the deposition temperature. The same measurements made on n-type films (not shown) yielded E_A of $\sim$50 meV and σ near 0.8 Scm^{-1} for all deposition temperatures.

Given these results, one might conclude that changes in either p-layer conductivity or doping efficiency are not the driving factor behind series resistance reduction. However, coplanar conductivity measurements probe the electrical transport properties laterally, when in operation it is the electrical transport perpendicular through the film that matters most. Indeed, μcSi is well-known to grow in a columnar structure surrounded by an amorphous matrix, in which current percolates freely in the direction of the crystalline columns but is impeded by the amorphous material during lateral transport. [24], [25] Therefore, coplanar measurements may not be sensitive to improvements in conductivity through the thickness of the films, which is the relevant direction for device operation. Considering this background, it is not possible to rule out an increased doping efficiency due to higher crystalline volume fraction in lower temperature cells using coplanar conductivity measurements alone.

To gain a better understanding of the mechanism by which enhanced crystallinity in the p-layer contributes to reduced series resistance in the final cell, we performed PC1D simulations in which electron affinity, bandgap, or doping concentration were varied in the p-type μc-Si:H layer. Fig. 5 displays the resulting FF of the simulated cells and the activation energy (E_A) values (i.e. the distance between the Fermi energy and the valence band maximum) for the free-standing p-layer in each condition. For each simulation, the intrinsic carrier concentration in the wafer was held constant at 3.6 x 10^{10} cm^{-3}, and when not varied the p-μcSi:H electron affinity was set to 4.05 eV, the bandgap was set to 1.2 eV, and the doping concentration was set to 4 x 10^{19} cm^{-3}.

In Fig. 5a-c, increasing the electron affinity, bandgap, or doping concentration of the p-layer each resulted in 1-2% gains in FF, similar to what was observed in the real devices when doped layer deposition temperature was lowered from 200°C. In panels (d)-(f), differing trends in activation energy for the free-standing p-layer were found depending on which property was varied. Increasing the electron affinity in (d) produced no change in activation energy, while increasing the bandgap in (e) resulted in an increase of $\sim$40 meV. Increasing doping concentration had the opposite effect on activation energy, yielding a decrease by 40 meV.

Comparing to the results shown in Figs. 1 and 4, it is possible that all three of these phenomena contribute to the reduction in series resistance observed for the lower temperature cells. An increasing electron affinity yields a reasonable reproduction of the experimental data, if the E_A values in Fig. 4b are taken to be essentially constant within the error of the measurement. Keeping in mind the earlier discussion on the limitations of lateral conductivity measurements of microcrystalline silicon, the simulations with varying p-layer doping also reasonably reproduce the data if we assume that an increased doping efficiency was missed by the dark conductivity measurements. However, with the data presented herein, we find that the best reproduction of the experimental trends in FF and E_A is seen with a simulated bandgap increase.

It is important to note that in these simulations, the bandgap shown is the mobility bandgap, defined by the energy level in each band tail at which the band tail states become dense enough to be effectively continuous. The mobility bandgap in microcrystalline silicon is known to exhibit a range of values, anywhere from 1.1-1.3 eV [26], which encompasses the range of simulated bandgaps in Fig. 5b. To say that a bandgap increase occurs in the p-type μc-Si:H when deposited at lower temperature, in fact refers to a decreasing density of band tail states at both the valence and conduction band, which results in the energy levels where they become effectively continuous moving farther apart [27]. We propose that this shift in the mobility bandgap would induce greater band bending in the c-Si wafer at the interface with the p-type contact (similar to the case of p-aSi [28]), leading to the reduced series resistance observed in the final cells.

Fig. 6 shows illuminated band diagrams of the p-type con-

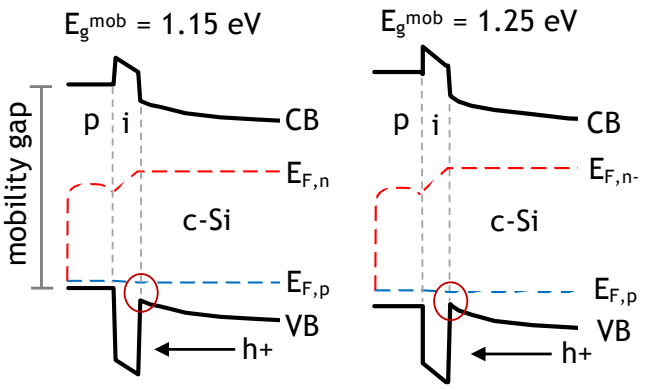

Fig. 6. Illuminated band diagrams from PC1D simulations for the p-type contact when the mobility gap of the p-μcSi:H is either 1.15 eV (left) or 1.25 eV (right). In each diagram, the quasi-Fermi level for electrons ($E_{F,n}$) is depicted as a dashed red line, and for holes ($E_{F,p}$) as a dashed blue line. CB and VB designate the conduction band and valence band of the c-Si wafer, respectively. Red circles in each diagram are intended to draw attention to the increased band bending induced when the mobility bandgap of the p-type layer increases from 1.15 eV to 1.25 eV.

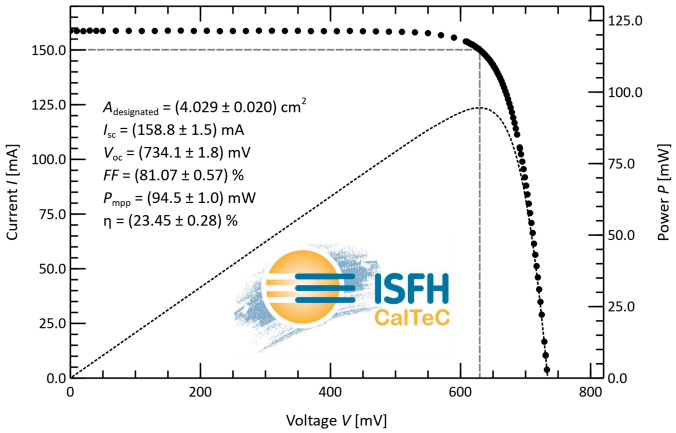

Fig. 7. Certified IV and power curves for an optimized SHJ solar cell prepared with 175 °C p-type μc-Si:H. Efficiency was certified by ISFH to be 23.45%.

tact at maximum power point constructed from the same PC1D simulations presented in Fig. 5b and e. The diagram on the left corresponds to the lowest bandgap point, E_g = 1.15 eV, and the diagram on the right corresponds to the highest bandgap point, E_g = 1.25 eV. In both cases, the E_g values represent the mobility bandgap as discussed above. Red circles at the valence band edge of the c-Si wafer where it makes contact with the intrinsic amorphous silicon demonstrate the enhanced band bending induced in the c-Si when the mobility gap of the p-type layer increases. Such an increase in band bending would lead to improved hole extraction by reducing the thermionic barrier formed by the intrinsic a-Si:H layer [29]–[31]. We propose that this effect best describes the changes observed when depositing the p-layer at lower temperature compared to deposition at 200 °C. This picture is consistent with the much better FF at low measurement temperatures (15 °C) displayed in Fig. 4a for low temperature devices, which provides an explanation for the observed reduction in R_s for low temperature cells compared to 200 °C cells (Fig. 1f). Moreover, we note that even if the mobility bandgap did not change, and instead the doping concentration increased (or indeed if these effects occurred simultaneously), the final result would be the same: band bending would be enhanced in the c-Si wafer, thus facilitating hole extraction at the p-type contact and reducing series resistance.

Finally, Fig. 7 displays the certified IV and power curves of an optimized, 4 cm^2 SHJ cell utilizing p-type μc-Si:H deposited at 175 °C. A single ITO layer was used on the front side as the sole anti-reflection scheme, and front-side metallization was screen-printed. Certified cell efficiency for this optimized device reached 23.45% with FF = 81.07%, J_{sc}= 39.41 mA/cm^2, V_{oc}= 734.1 mV, and P_{mpp}= 94.5 mW. The increase in FF achieved for this champion cell is approximately 2% absolute compared to the best cells in Fig. 1, which is due to fine-tuning of the total process flow and the use of a thinner wafer. Ultimately, this work demonstrates that enhancing crystallinity in p-type μc-Si:H is an effective strategy for reducing parasitic absorption and series resistance losses in SHJ solar cells.

IV. Conclusion

By lowering the deposition temperature of doped μc-Si:H contact layers in SHJ solar cells, we found that all metrics for device performance were improved. This was explained as resulting mostly from the front p-type contact layer, for which a marked increase in crystalline volume fraction was observed at growth temperatures <200 °C. This enhancement in crystallinity led to two key improvements: (1) parasitic absorption at the front contact was reduced due to greater transparency in the p-type μc-Si:H deposited at <200°C, as evidenced by short wavelength gains in EQE and a higher energy E_{04} for these layers; and (2) hole extraction at the p-type contact was improved, as deduced from PC1D simulations and lower R_s overall for low temperature cells. With this method, we achieved a certified cell efficiency of 23.45%, and highlighted the importance of band bending considerations when optimizing SHJ solar cell designs.

Appendix A

For bound multi-model fits of the ellipsometry and UV-Vis-NIR transmission spectra discussed in Fig. 3, the Kato-Adachi dispersion formula was used [19]:

$$\epsilon = \epsilon_\infty + \epsilon_1 + \epsilon_2 + \epsilon_3 + \epsilon_4$$

where:

$$\epsilon_1 = \frac{A_0}{E_0^{1.5}} \cdot \frac{2 - \sqrt{1+\chi} - \sqrt{1-\chi}}{\chi^2}$$

$$\epsilon_2 = -\frac{B_1}{\xi^2} \cdot \ln(1 - \xi^2)$$

$$\epsilon_3 = \frac{B_{1x}}{E_1 - E - i \cdot \Gamma_1}$$

$$\epsilon_4 = \frac{C}{1 - (\frac{E}{E_2})^2 - i \cdot \frac{E}{E_2} \cdot \Gamma_2}$$

$$\chi = \frac{E + i \cdot \Gamma_0}{E_0}$$
$$\xi = \frac{E + i \cdot \Gamma_1}{E_1}$$

Starting values for each variable were taken from the polycrystalline silicon material dispersion ("p-Si_fine_grain_KA.dsp") included with the DeltaPsi2 software from Horiba. The global model used for each film is depicted in Fig. 8

Fig. 8. Schematic of the global model used for bound multi-model fitting ellipsometry and transmission spectra of p-type μc-Si:H layers on glass.

The glass dispersion was taken from fitting an ellipsometry measurement of the glass substrate. A roughness layer was included by setting the top layer to be composed of the void dispersion and the same Kato-Adachi dispersion used for the film layer, at a fixed percentage of 50% each.

ACKNOWLEDGMENT

This project has received funding from the European Union's Horizon 2020 research and innovation programme under Grant Agreement No. 727523 (NextBase). ANF received funding from the Horizon 2020 Marie Skłodowska-Curie Actions under Grant Agreement No. 792720 (CLAReTE). Funding from the Swiss National Science Foundation (SNF) through the Ambizione Energy grant "ICONS" is also acknowledged. The authors would like to thank Christophe Allebe and Fabien Debrot from CSEM for high quality wet-processing of the silicon wafers, and Nicolas Badel from CSEM for screen printing. Additional thanks to Luca Antognini of EPFL for the MatLab code used to determine crystalline volume fraction from Raman spectroscopy, and to Jean Cattin of EPFL for timely repairs and helpful troubleshooting of the temperature-dependent JV instrument.

REFERENCES

[1] J. Haschke, O. Dupré, M. Boccard, and C. Ballif, "Silicon heterojunction solar cells: Recent technological development and practical aspects - from lab to industry," *Solar Energy Materials and Solar Cells*, vol. 187, pp. 140–153, Dec. 2018.

[2] K. Yoshikawa, H. Kawasaki, W. Yoshida, T. Irie, K. Konishi, K. Nakano, T. Uto, D. Adachi, M. Kanematsu, H. Uzu, and K. Yamamoto, "Silicon heterojunction solar cell with interdigitated back contacts for a photoconversion efficiency over 26%," *Nature Energy*, vol. 2, no. 5, p. 17032, Mar. 2017.

[3] J. Melskens, B. W. H. van de Loo, B. Macco, L. E. Black, S. Smit, and W. M. M. Kessels, "Passivating contacts for crystalline silicon solar cells: from concepts and materials to prospects," *IEEE Journal of Photovoltaics*, vol. 8, no. 2, pp. 373–388, Mar. 2018.

[4] M. Mews, A. Lemaire, and L. Korte, "Sputtered tungsten oxide as hole contact for silicon heterojunction solar cells," *IEEE Journal of Photovoltaics*, vol. 7, no. 5, pp. 1–7, Sep. 2017.

[5] G. Nogay, J. P. Seif, Y. Riesen, A. Tomasi, Q. Jeangros, N. Wyrsch, F.-J. Haug, S. De Wolf, and C. Ballif, "Nanocrystalline silicon carrier collectors for silicon heterojunction solar cells and impact on low-temperature device characteristics," *IEEE Journal of Photovoltaics*, vol. 6, no. 6, pp. 1654–1662, Nov. 2016.

[6] J. P. Seif, A. Descoeudres, G. Nogay, S. Hanni, S. M. de Nicolas, N. Holm, J. Geissbuhler, A. Hessler-Wyser, M. Duchamp, R. E. Dunin-Borkowski, M. Ledinsky, S. De Wolf, and C. Ballif, "Strategies for doped nanocrystalline silicon integration in silicon heterojunction solar cells," *IEEE Journal of Photovoltaics*, vol. 6, no. 5, pp. 1132–1140, Sep. 2016.

[7] L. G. Gerling, S. Mahato, A. Morales-Vilches, G. Masmitja, P. Ortega, C. Voz, R. Alcubilla, and J. Puigdollers, "Transition metal oxides as hole-selective contacts in silicon heterojunctions solar cells," *Solar Energy Materials and Solar Cells*, vol. 145, pp. 109–115, 2016.

[8] L. Mazzarella, S. Kirner, B. Stannowski, L. Korte, B. Rech, and R. Schlatmann, "p-type microcrystalline silicon oxide emitter for silicon heterojunction solar cells allowing current densities above 40 mA/cm^2," *Applied Physics Letters*, vol. 106, no. 2, p. 023902, Jan. 2015.

[9] M. Bivour, J. Temmler, H. Steinkemper, and M. Hermle, "Molybdenum and tungsten oxide: High work function wide band gap contact materials for hole selective contacts of silicon solar cells," *Solar Energy Materials and Solar Cells*, vol. 142, pp. 34–41, 2015.

[10] C. Battaglia, S. M. De Nicolas, S. De Wolf, X. Yin, M. Zheng, C. Ballif, and A. Javey, "Silicon heterojunction solar cell with passivated hole selective MoO_x contact," *Applied Physics Letters*, vol. 104, no. 11, p. 113902, 2014.

[11] O. Madani Ghahfarokhi, K. von Maydell, and C. Agert, "Enhanced passivation at amorphous/crystalline silicon interface and suppressed Schottky barrier by deposition of microcrystalline silicon emitter layer in silicon heterojunction solar cells," *Applied Physics Letters*, vol. 104, no. 11, p. 113901, Mar. 2014.

[12] T. Watahiki, T. Furuhata, T. Matsuura, T. Shinagawa, Y. Shirayanagi, T. Morioka, T. Hayashida, Y. Yuda, S. Kano, Y. Sakai, H. Tokioka, Y. Kusakabe, and H. Fuchigami, "Rear-emitter Si heterojunction solar cells with over 23% efficiency," *Applied Physics Express*, vol. 8, no. 2, p. 021402, Feb. 2015.

[13] L. Mazzarella, S. Kirner, O. Gabriel, S. S. Schmidt, L. Korte, B. Stannowski, B. Rech, and R. Schlatmann, "Nanocrystalline silicon emitter optimization for Si-HJ solar cells: Substrate selectivity and CO_2 plasma treatment effect," *physica status solidi (a)*, vol. 214, no. 2, p. 1532958, Feb. 2017.

[14] N. Pellaton Vaucher, B. Rech, D. Fischer, S. Dubail, M. Goetz, H. Keppner, N. Wyrsch, C. Beneking, O. Hadjadj, V. Shklover, and A. Shah, "Controlled nucleation of thin microcrystalline layers for the recombination junction in a-Si stacked cells," *Solar Energy Materials and Solar Cells*, vol. 49, no. 1–4, pp. 27–33, Dec. 1997.

[15] M. Boccard, R. Monnard, L. Antognini, and C. Ballif, "Silicon oxide treatment to promote crystallinity of p-type microcrystalline layers for silicon heterojunction solar cells," in *AIP Conference Proceedings*, vol. 1999, no. 1, p. 040003, Aug. 2018.

[16] P. Basore and D. Clugston, "PC1D version 4 for Windows: from analysis to design," in *25th IEEE Photovoltaic Specialists Conference*, pp. 377–381, 1996.

[17] C. Droz, E. Vallat-Sauvain, J. Bailat, L. Feitknecht, J. Meier, and A. Shah, "Relationship between Raman crystallinity and open-circuit voltage in microcrystalline silicon solar cells," *Solar Energy Materials and Solar Cells*, vol. 81, no. 1, pp. 61–71, Jan. 2004.

[18] D. Pysch, A. Mette, and S. Glunz, "A review and comparison of different methods to determine the series resistance of solar cells," *Solar Energy Materials and Solar Cells*, vol. 91, no. 18, pp. 1698–1706, Nov. 2007.

[19] H. Kato, S. Adachi, H. Nakanishi, and K. Ohtsuka, "Optical properties of $(Al_xGa_{1-x})_{0.5}In_{0.5}P$ quaternary alloys," *Japanese Journal of Applied Physics*, vol. 33, no. Part 1, No.1A, pp. 186–192, Jan. 1994.

[20] E. Fathi, Y. Vygranenko, M. Vieira, and A. Sazonov, "Boron-doped nanocrystalline silicon thin films for solar cells," *Applied Surface Science*, vol. 257, no. 21, pp. 8901–8905, Aug. 2011.

[21] S. Zhang and X. Zeng, "Influence of band gap of p-type hydrogenated nanocrystalline silicon layer on the short-circuit current density in thin-film silicon solar cells," *Journal of Semiconductors*, vol. 38, no. 11, p. 114007, Nov. 2017.

[22] N. Tarjudin, I. Sumpono, and S. Sakrani, "Optical properties of nanocrystalline silicon thin films in wider regions of wavelength," *Journal of Science and Technology*, vol. 4, no. 1, 2012.

[23] J. Rath and R. Schropp, "Incorporation of p-type microcrystalline silicon films in amorphous silicon based solar cells in a superstrate structure," *Solar Energy Materials and Solar Cells*, vol. 53, no. 1–2, pp. 189–203, May 1998.

[24] D. Azulay, I. Balberg, V. Chu, J. P. Conde, and O. Millo, "Current routes in hydrogenated microcrystalline silicon," *Physical Review B*, vol. 71, no. 11, p. 113304, Mar. 2005.

[25] H. Scher and R. Zallen, "Critical density in percolation processes," *Journal of Chemical Physics*, vol. 53, pp. 3759–3761, 1970.

[26] B. Yan, G. Yue, L. Sivec, C.-S. Jiang, Y. Yan, K. Alberi, J. Yang, and S. Guha, "On the bandgap of hydrogenated nanocrystalline silicon thin films," in *35th IEEE Photovoltaic Specialists Conference*, Jun. 2010, pp. 003755–003760.

[27] R. Carius, T. Merdzhanova, S. Klein, and F. Finger, "Band tail states in microcrystalline silicon solar cells probed by photoluminescence and open circuit voltage," *Journal of Optoelectronics and Advanced Materials*, vol. 7, no. 1, pp. 121–128, 2005.

[28] J. Temmler, M. Bivour, H. Steinkemper, and M. Hermle, "Boron doped a-SiC:H front layers for silicon heterojunction cells," in *29th European Photovoltaic Solar Energy Conference and Exhibition*, Amsterdam, Netherlands, 2014.

[29] R. Biron, C. Pahud, F.-J. Haug, J. Escarré, K. Söderström, and C. Ballif, "Window layer with p-doped silicon oxide for high V_{oc} thin-film silicon n-i-p solar cells," *Journal of Applied Physics*, vol. 110, no. 12, p. 124511, Dec. 2011.

[30] B. E. Pieters, S. Schicho, and H. Stiebig, "Characterization of the mobility gap in μc-Si:H pin devices," *MRS Proceedings*, vol. 1066, pp. 1066–A04–03, Jan. 2008.

[31] S. Hamma and P. Roca Cabarrocas, "Determination of the mobility gap of microcrystalline silicon and of the band discontinuities at the amorphous/ microcrystalline silicon interface using *in situ* Kelvin probe technique," *Applied Physics Letters*, vol. 74, p. 3218, 1999.